

Supporting Information

for *Adv. Funct. Mater.*, DOI: 10.1002/adfm.202205214

Unprecedented Multifunctionality in 1D Nb_{1-x}Ta_xS₃
Transition Metal Trichalcogenide Alloy

*Zahra Hemmat, Alireza Ahmadiparidari, Shuxi Wang,
Khagesh Kumar, Michael Zepeda, Chengji Zhang,
Naveen Dandu, Sina Rastegar, Leily Majidi, Ahmad
Jaradat, Anh Ngo, Katsuyo Thornton, Larry A. Curtiss,
Jordi Cabana,* Zhehao Huang,* and Amin Salehi-Khojin**

Supplementary information

Unprecedented Multifunctionality in One-Dimensional Nb_{1-x}Ta_xS₃ Transition Metal Trichalcogenide Alloy

Z. Hemmat^{1,§}, A. Ahmadiparidari^{1,§}, S. Wang^{2,§}, K. Kumar³, M. Zepeda⁴, C. Zhang¹, N. Dandu⁴, S. Rastegar¹, L. Majidi¹, A. Jaradat¹, A. T. Ngo⁴, K. Thornton⁵, L. A. Curtiss⁶, J. Cabana^{3,*}, Z. Huang^{7,*}, A. Salehi-Khojin^{1,*}

¹Department of Mechanical and Industrial Engineering, University of Illinois at Chicago, Chicago, IL, 60607, USA.

²Department of Physics, University of Illinois at Chicago, Chicago, IL, 60607, USA.

³Department of Chemistry, University of Illinois at Chicago, Chicago, IL, 60607, USA.

⁴Department of Chemical Engineering, University of Illinois at Chicago, Chicago, IL, 60607, USA.

⁵Department of Materials Science and Engineering, University of Michigan, Ann Arbor, MI 48109-2136, USA.

⁶Materials Science Division, Argonne National Laboratory, Lemont, IL 60439, USA.

⁷Department of Materials and Environmental Chemistry, Stockholm University, Stockholm, SE-106 91, Sweden.

[§]These authors contributed equally to this work.

*Corresponding authors: salehikh@uic.edu, zhehao.huang@mmk.su.se, jcabana@uic.edu

[§]These authors contributed equally to this work.

*Corresponding authors: salehikh@uic.edu, zhehao.huang@mmk.su.se, jcabana@uic.edu

Supplementary information

Table of Contents:

- S1. Synthesis of the nanofiber alloy**
- S2. Diameter distribution of nanofibers**
- S3. Energy Dispersive X-Ray Spectroscopy (EDX)**
- S4. Transmission electron microscopy (TEM) measurement**
- S5. Atomic force microscopy (AFM) characterization of devices**
- S6. Electrical characteristics of nanofiber devices**
- S7. Mechanical characteristics of the synthesized nanofibers**
- S8. Electrochemical CO₂ conversion experiments**
- S9. X-ray photoelectron spectroscopy (XPS)**
- S10. Application comparison of Nb_{0.5}Ta_{0.5}S₃, NbS₃ and TaS₃**
- S11. DFT calculations**

S1. Synthesis of the nanofiber alloy

Figure S1 shows the optical image of the quartz ampule and SEM images after the synthesis process which is covered by dense forest of $\text{Nb}_{1-x}\text{Ta}_x\text{S}_3$ whiskers.

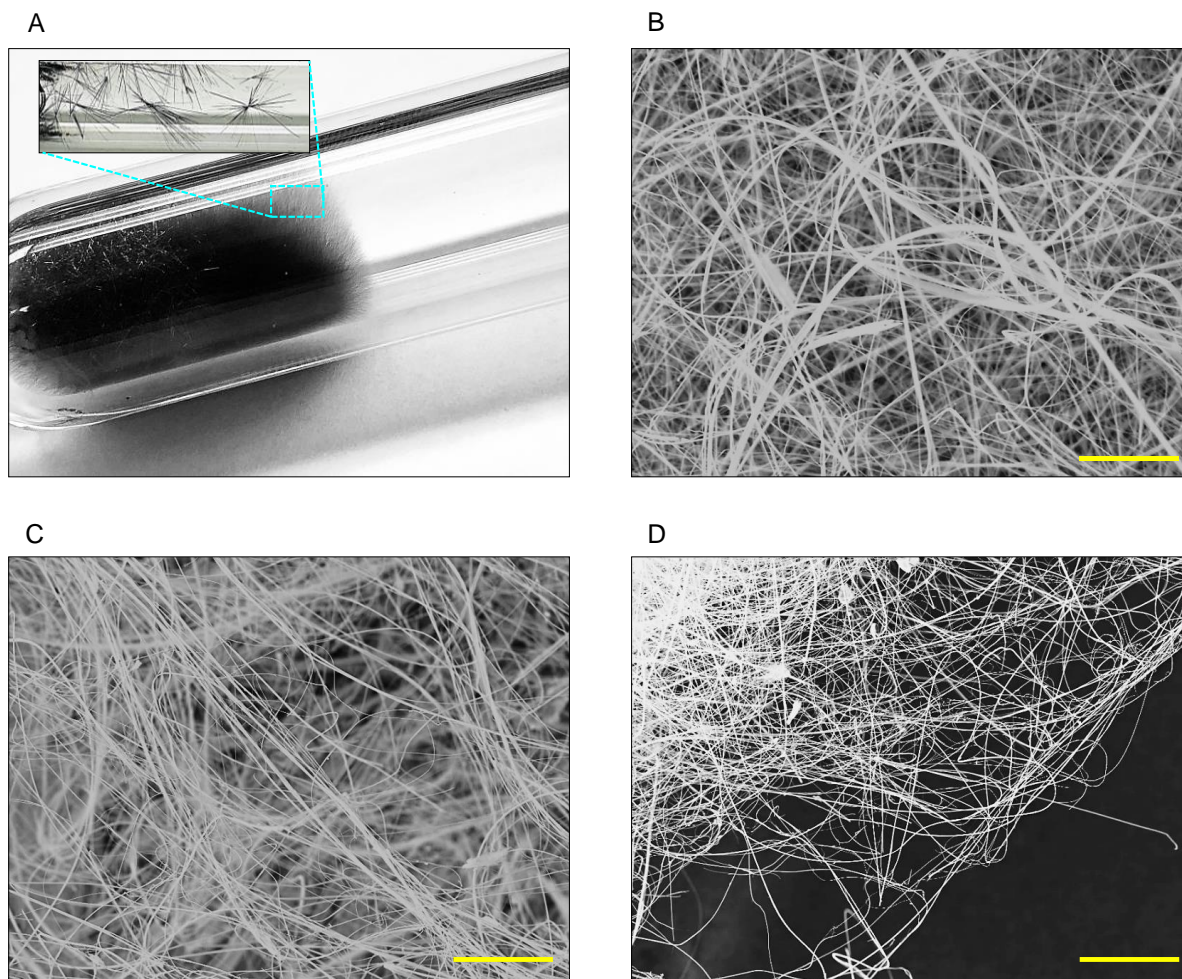


Figure S1. (A) Reaction ampule after synthesis showing $\text{Nb}_{1-x}\text{Ta}_x\text{S}_3$ whiskers. (B-D) SEM images of long belt-like $\text{Nb}_{1-x}\text{Ta}_x\text{S}_3$ nanofibers (scale bar: 50 μm).

S2. Diameter distribution of nanofibers

Figure S2 shows the diameter distribution obtained from SEM images of three various synthesis batch. The distributions from these spots show average width of ≈ 250 -300 nm.

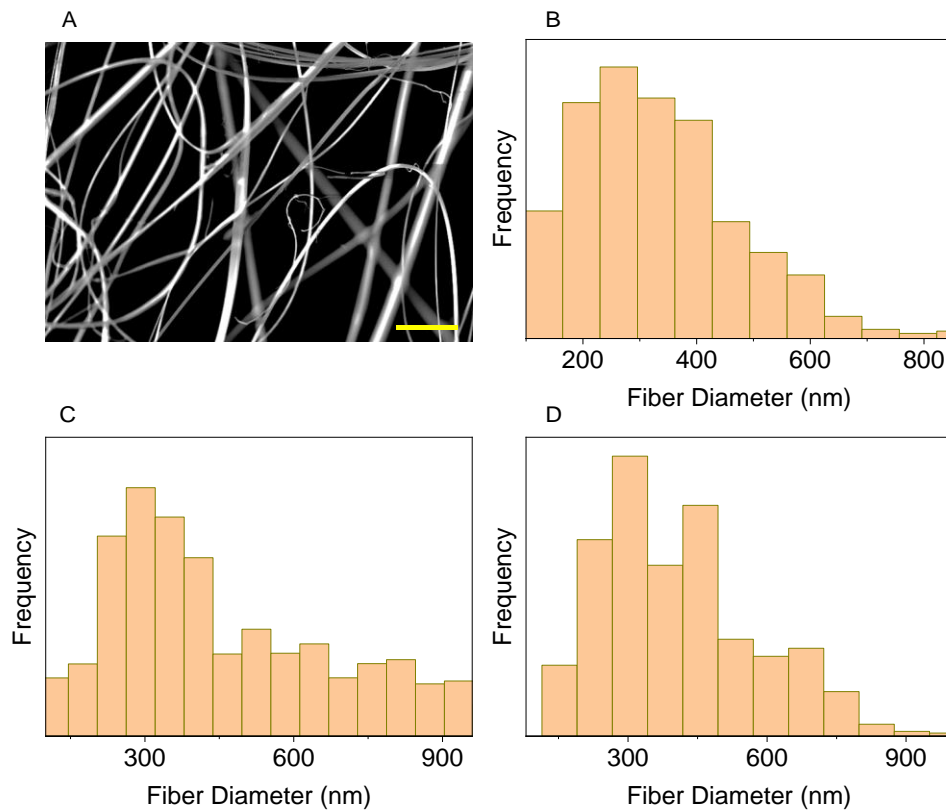


Figure S2. Diameter distribution of nanofibers. (A) SEM image of belt-like $\text{Nb}_{1-x}\text{Ta}_x\text{S}_3$ nanoribbons (scale bar: 5 μm). (B-D) Diameter measurements show average width of ~ 250 -300 nm.

S3. Energy Dispersive X-Ray Spectroscopy (EDX)

Figures S3 represent the summary of Scanning Electron Microscopy (SEM)-EDX characterization for $\text{Nb}_{1-x}\text{Ta}_x\text{S}_3$ nanofiber.

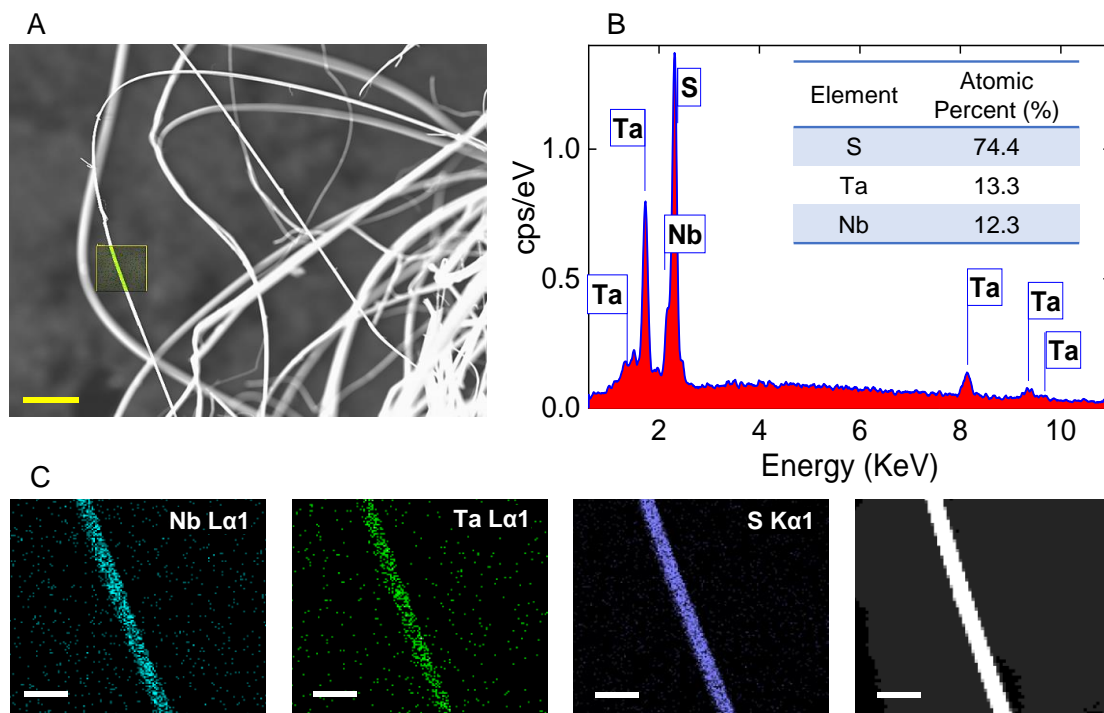


Figure S3. SEM-EDX characterization of $\text{Nb}_{1-x}\text{Ta}_x\text{S}_3$ alloy. (A) SEM image of the fibers (scale bar: 10 μm). (B) EDX spectrum acquired from the area marked by a square in (A). The quantification results are presented in the table, showing the average stoichiometry ratio of $\text{Nb}_{0.5}\text{Ta}_{0.5}\text{S}_3$. (C) Full EDX composition mapping of the detected elements (scale bars: 2 μm).

S4. Transmission electron microscopy (TEM) measurement

Figure S4 presents the 3D reciprocal lattice reconstructed from the cRED data and 2D slice cuts showing that the nanofibers are crystallized in a monoclinic crystal system.^[1-3]

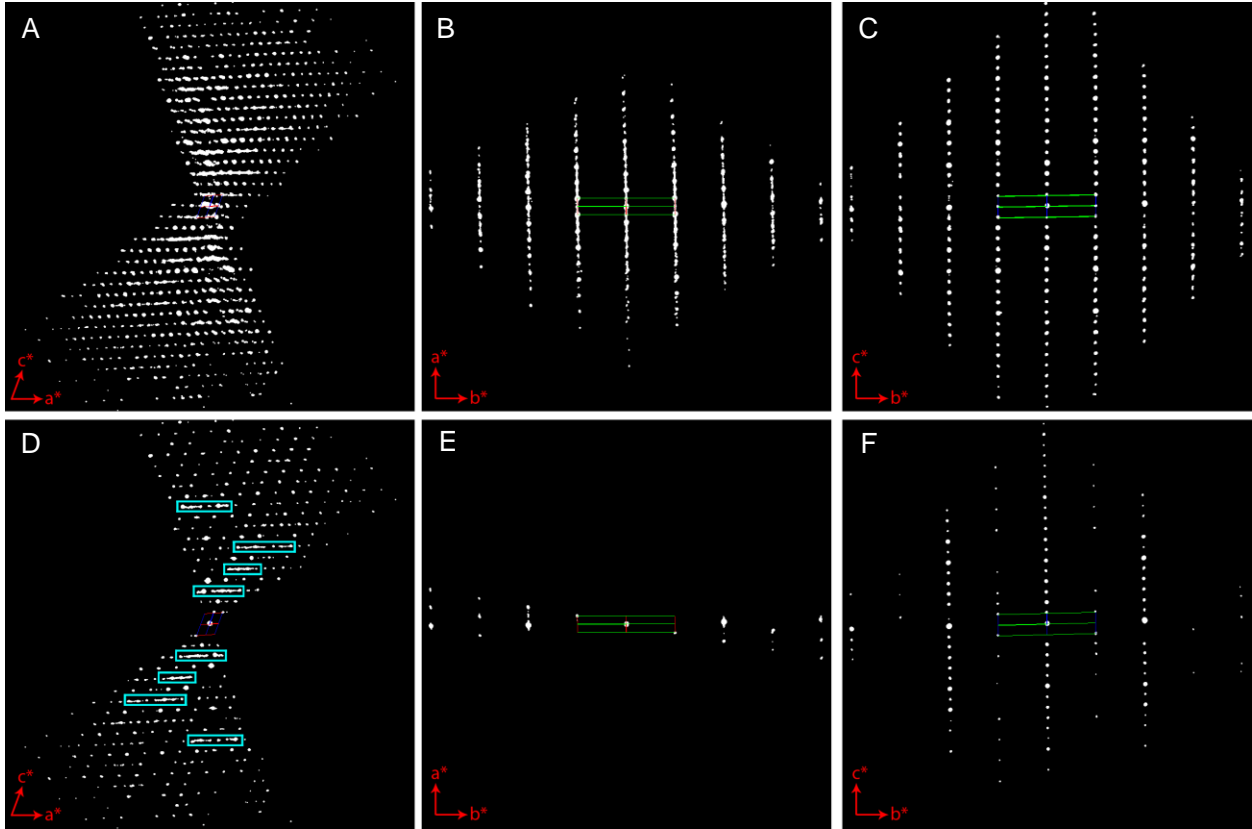


Figure S4. The reconstructed 3D reciprocal lattice of $\text{Nb}_{1-x}\text{Ta}_x\text{S}_3$ nanofiber viewed along the (A) [010], (B) [001], and (C) [100] directions. 2D slice cuts from the reconstructed 3D reciprocal lattice show the (D) $h0l$, (E) $hk0$ and (F) $0kl$ planes. Diffused scattering can be observed in the data, which indicates disordered structure of $\text{Nb}_{1-x}\text{Ta}_x\text{S}_3$ nanofibers. Some spots violating reflection conditions can be observed, which is resulted from multiple scattering.

S5. Atomic force microscopy (AFM) characterization of devices

AFM technique was employed to find the thickness and width of the tested fibers. **Figure S5** shows the AFM images of five representative fabricated devices. AFM characterization shows thicknesses in the range of 8 to 40 nm.

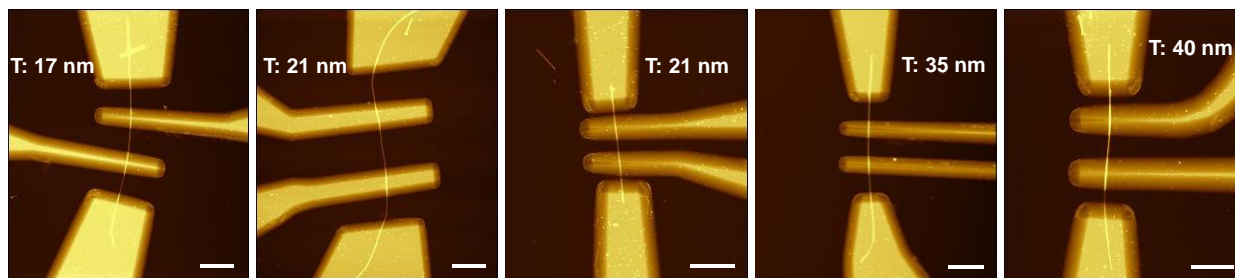


Figure S5. AFM micrograph of representative tested devices fabricated on mechanically exfoliated nanofibers (Scale bar is 5 μm).

S6. Electrical characteristics of nanofiber devices

To characterize the electrical properties of the synthesized nanofiber alloy, the fibers were mechanically exfoliated using polydimethylsiloxane (PDMS) stamp and were transfer onto a SiO_2/Si (≈ 300 nm/0.5 mm) substrate for electrical measurements. **Figure S6** shows the resistivity versus temperature for different devices with various thicknesses. Resistivity measurements verify phase transition associated with the charge density wave (CDW) states for all the tested devices. **Table S1** also summarize the electrical breakdown characteristics of the tested devices in **Figure 3D**.

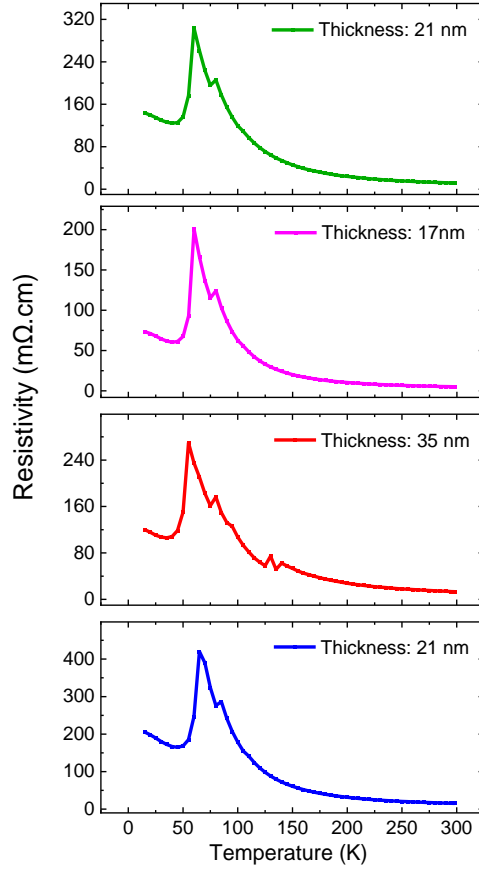


Figure S6. Temperature dependence of resistivity for $\text{Nb}_{1-x}\text{Ta}_x\text{S}_3$ nanofibers with various thicknesses.

Table S1. Maximum current density and breakdown voltage of $\text{Nb}_{1-x}\text{Ta}_x\text{S}_3$ nanofibers.

Device #	Thickness (nm)	Width (nm)	Length (μm)	Maximum Current Density (MA/cm^2)	Breakdown Voltage (V)
1	8	400	1.8	32.26	4.4
2	25	180	2.5	10.56	4.6
3	25	300	1.7	14.96	6.7
4	40	400	5.5	13.38	29.2
5	35	200	4.8	4.98	16.7
6	17	250	3.5	10.37	11.3
7	21	200	10.4	8.37	38.8
8	21	200	1.7	7.96	4.7

S7. Mechanical characteristics of the synthesized nanofibers

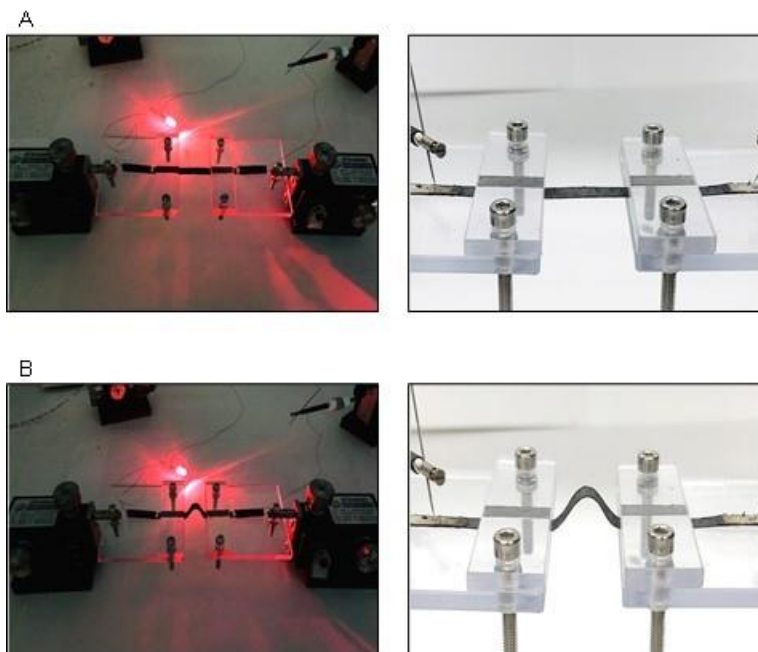


Figure S7. Mechanical stability of the $\text{Nb}_{1-x}\text{Ta}_x\text{S}_3$ nanofibers

S8. Electrochemical CO_2 conversion experiments

a. Electrochemical electrode preparation, setup and calculations:

In order to prepare electrodes for electrochemical experiments, first 0.2 g of $\text{Nb}_{1-x}\text{Ta}_x\text{S}_3$ was dissolved in 70 mL of IPA and was set to be exfoliated through liquid tip sonication for about 15 hours. Then the solution was centrifuged and the 70% of the supernatant was collected. The obtained solution was spray coated on 25BC gas diffusion electrodes (GDL) purchased from Sigracet until it reached 0.2 mg/cm^2 of catalyst loading.

All the electrochemical measurements were operated by Voltalab potentiostat (PGZ100). In this setup we used Ag/AgCl and Pt wire as reference and counter electrodes, respectively. 1M KOH (Fisher-Scientific) was dissolved in water serving as the electrolyte. For CV experiments, the solution was purged with UHP CO_2 for 30 minutes until the pH of the electrolyte reached to

~7.6. For CA tests, we kept purging CO₂ at a very low rate to avoid disturbance during operation and depletion of CO₂ throughout long-term experiments. All the potentials were converted to RHE using: V vs RHE = V vs Ag/AgCl + 0.210 + 0.0592×pH. The reported potentials were iR corrected for all experiments.

Faradaic Efficiency (FE) of CO and H₂ were calculated using the following equation:

$$FE_i = \frac{nFn_i}{It} \times 100,$$

where FE_i is Faradaic efficiency of i (CO or H₂), n is the number of electrons transferred, F is the Faraday constant (96485), n_i is the number of moles of i (CO or H₂) produced in time t and I is current. n_i was calculated from the integration of the number of moles obtained from DEMS results.

Turnover number (TON) are calculated using following equation:

$$TON = \frac{n_{CO}}{n_{catalyst}}$$

Catalyst number of moles were calculated based on geometric surface area (2×2cm²) and loading (0.2 mg/cm²).

b. Differential electrochemical mass spectroscopy (DEMS)

Gas detection during electrochemical tests was performed by DEMS. The methods and details are discussed elsewhere.^[4] In detail, the cell was calibrated for H₂ and CO as a function of relative pressure (**Figure S8**). CA and CV tests were coupled with simultaneous online DEMS. The scan rate during CV experiments was 1mV/sec. The characterization of gases via DEMS was done for 60 minutes during CA tests.

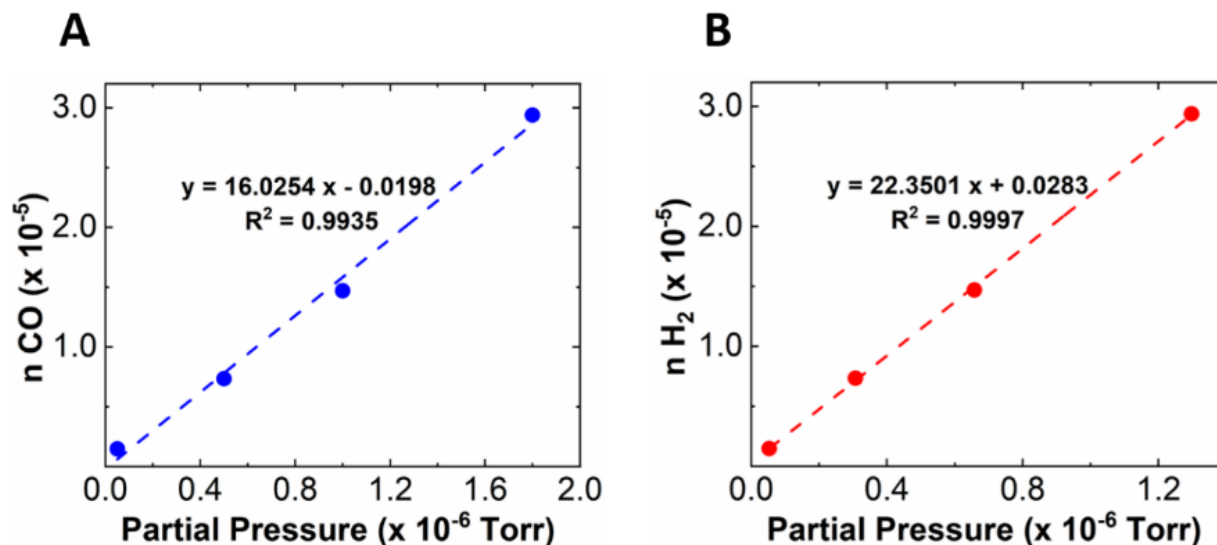


Figure S8. Calibration curves used to characterize (A) CO and (B) H₂

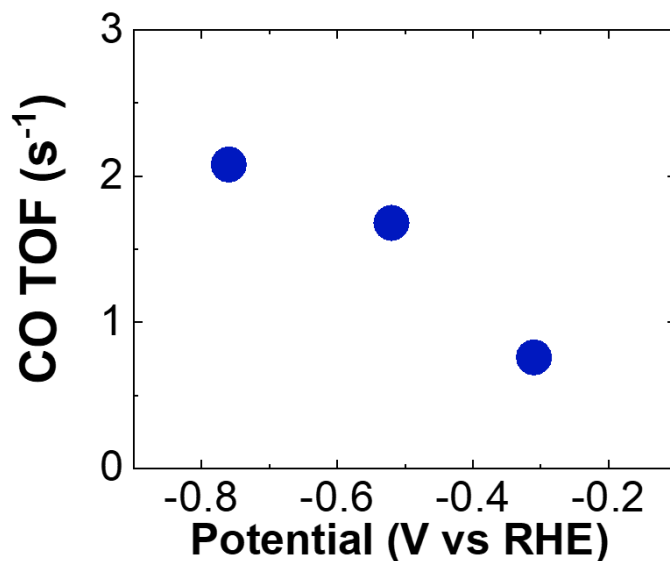


Figure S9. CO TOF calculated for Ag particles coated on a gas diffusion layer.

Figure S10 depicts the evolution of O₂ gas during charge process. Our calculations show that the number of electrons consumed per oxygen equals to 2.07 (e⁻/mole O₂) which corresponds to decomposition of Li₂O₂. We note that there is no sign of evolved water or CO₂ compounds, further confirming the Li₂O₂ formation as the only product of the discharge process. Our DEMS

results indicate that 0.248 mg of Li_2O_2 formed which results in 74% capacity utilization as calculated by the following equations:

$$\frac{3.6}{F \cdot b} \times M = m_{\text{Li}_2\text{O}_2} \text{ [mg/mAh]}$$

Where $m_{\text{Li}_2\text{O}_2}$ is the weight of Li_2O_2 product, F is the Faraday constant (96485), b is the number of transferred electrons (here is 2.07), and M is the molecular weight of the product (45.88 g/mole). Using calculated 0.248 mg of produced Li_2O_2 in the following equation results in a normalized capacity of 862 mAh per total mass of cathode material and discharge product. Dividing this value by theoretical capacity of Li- O_2 battery ($1168 \text{ mAh}_{\text{Li}_2\text{O}_2}^{-1}$) will result in 74% of capacity utilization (depth of discharge) at the current density of 0.3 mA/g.

$$Q_{\text{tot}} \left(\frac{\text{mAh}}{\text{g}} \right) = \frac{Q \text{ (mAh)}}{m_{\text{total}}} = \frac{Q}{(m_{\text{Li}_2\text{O}_2} + m_{\text{catalyst}})}$$

$$Q_{\text{tot}} = \frac{0.3 \text{ (mAh)}}{0.248 + 0.1 \text{ (mg)}} = 862 \text{ mAh/g}$$

$$\frac{862}{1168} \text{ mAh} \times 100 = 74\%$$

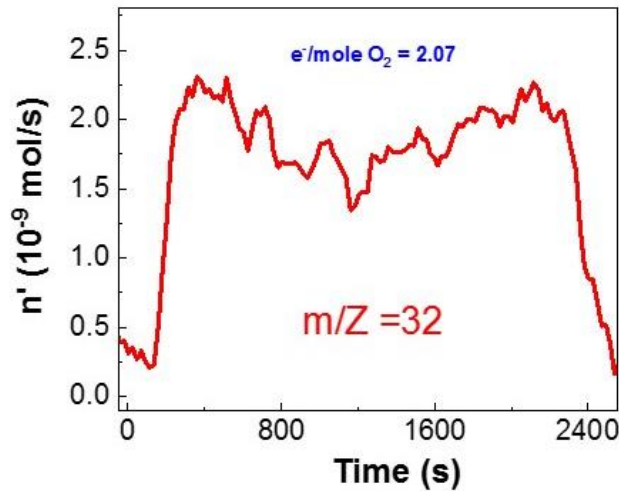


Figure S10. Oxygen evolution signal during charging process of the battery using a 0.5 mA/cm²

S9. X-ray photoelectron spectroscopy (XPS)

To further validate the formation of Li_2O_2 after the discharge process we performed differential XPS experiment. We conducted XPS on a discharged cathode under the same conditions that batteries were operated before. Figure S11 shows XPS Li 1s and O 1s spectra showing peaks at 55.03 eV and 531.7 eV, respectively, denoting the formation of Li_2O_2 .

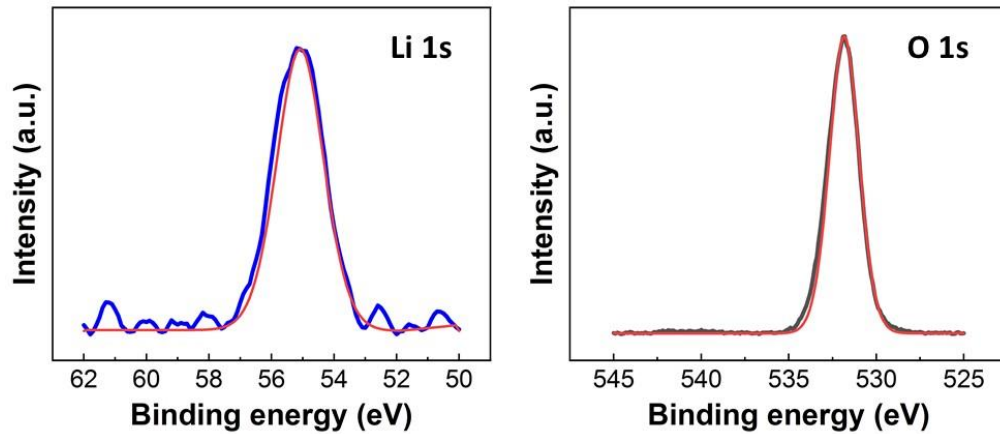


Figure S11- XPS results of the cathode after the discharge including O 1s and Li 1s spectra

S10. Comparison of $\text{Nb}_{0.5}\text{Ta}_{0.5}\text{S}_3$, NbS_3 and TaS_3

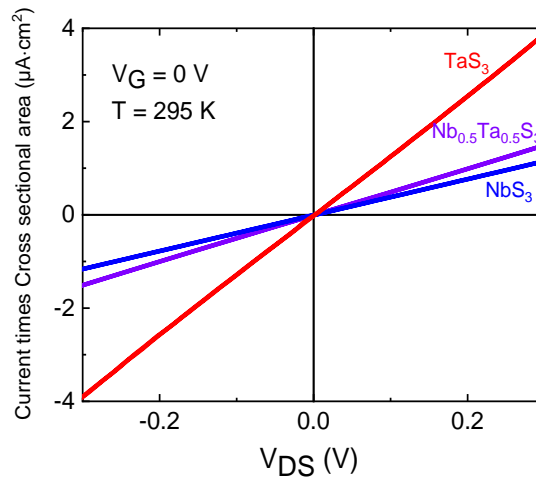


Figure S12. Transport characteristics of FET device based on individual nanofiber of $\text{Nb}_{0.5}\text{Ta}_{0.5}\text{S}_3$, NbS_3 and TaS_3 ; Source-drain current (I_{DS}) multiply by cross sectional area of device channel as a function of source-drain voltage (V_{DS}).

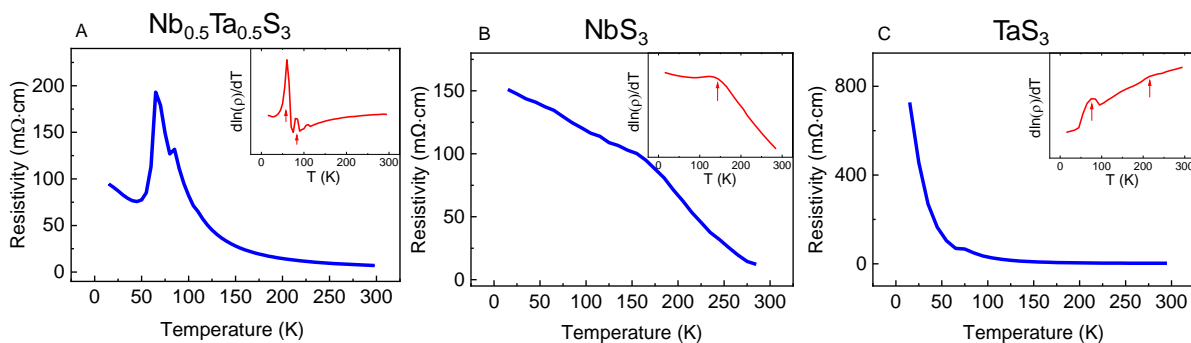


Figure S13. Temperature dependent resistivity of individual (A) $\text{Nb}_{0.5}\text{Ta}_{0.5}\text{S}_3$ (B) NbS_3 and (C) TaS_3 nanofiber at 15–295 K temperatures range. Inset: $d(\ln\rho)/dT$ as a function of temperature for nanofiber. The arrows point to the local maxima in each case.

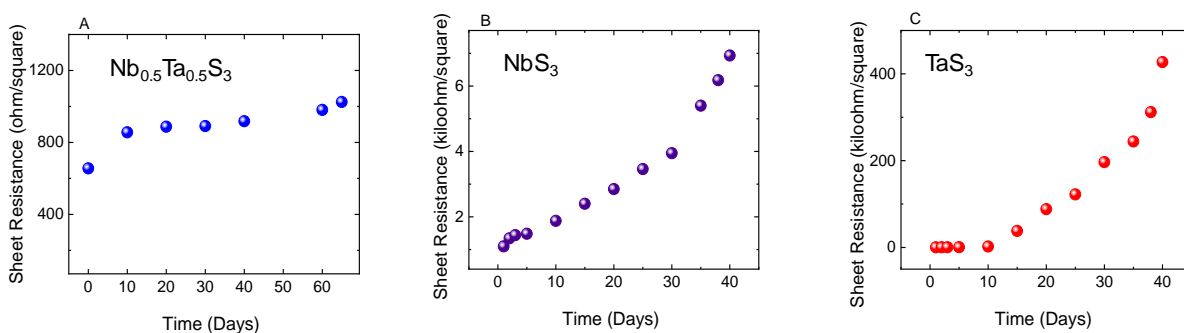


Figure S14. Air-stability of sheet resistance of (A) $\text{Nb}_{0.5}\text{Ta}_{0.5}\text{S}_3$ (B) NbS_3 and (C) TaS_3 thin films at ambient condition versus time.

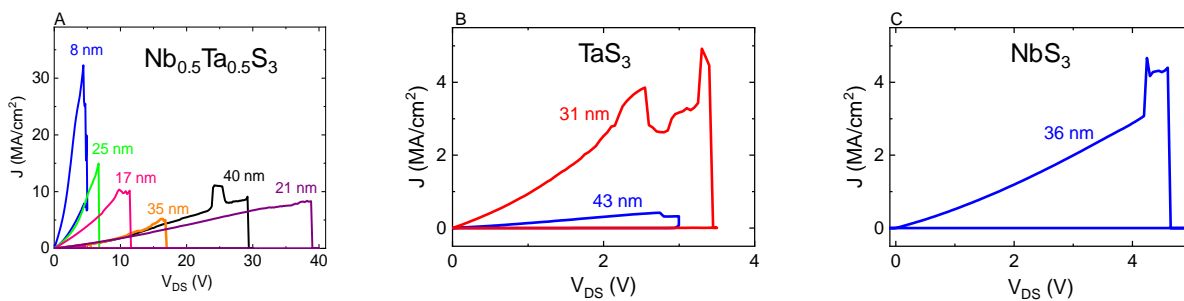


Figure S15. Breakdown current density versus voltage characteristics of individual nanofiber of (A) $\text{Nb}_{0.5}\text{Ta}_{0.5}\text{S}_3$, and (B) TaS_3 , and (C) NbS_3 .

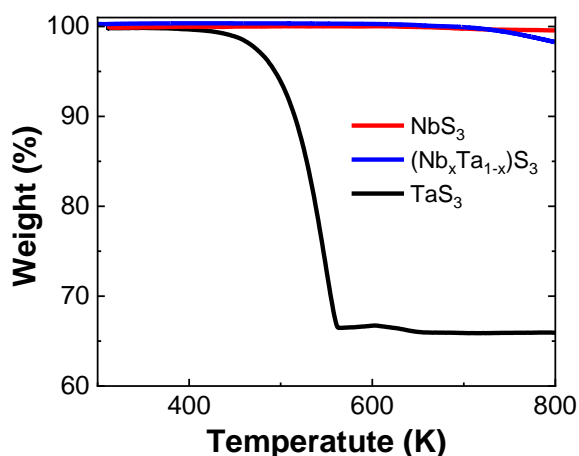


Figure S16. TGA curves for NbS_3 , TaS_3 and $\text{Nb}_x\text{Ta}_{1-x}\text{S}_3$ under Nitrogen at a 10 K min^{-1} heating rate.

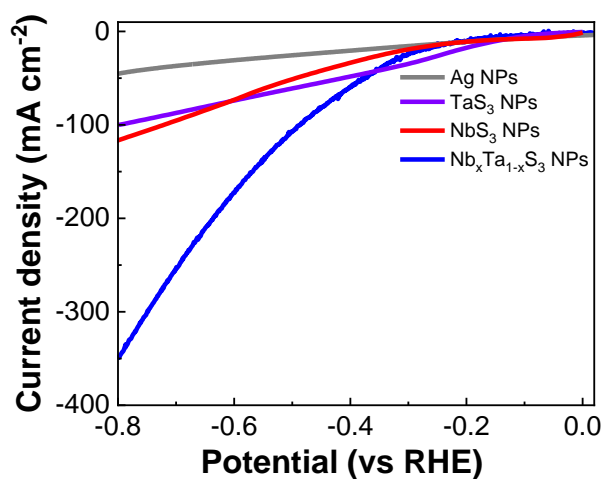


Figure S17. LSV test at 50mV/s scan rate for Ag nanoparticles, TaS_3 , NbS_3 and $\text{Nb}_x\text{Ta}_{1-x}\text{S}_3$ in 1 M KOH and CO_2 saturated aqueous media.

To assess the possible phase changes throughout the electrochemical CO_2 reduction reaction (CO_2RR), we performed XRD before and after one-hour chronoamperometry experiment. As shown in Figure S18, the diffraction pattern of $\text{Nb}_{0.5}\text{Ta}_{0.5}\text{S}_3$ before and after the catalysis match well with that of the liquid exfoliated samples (with matches at ~ 12.6 , ~ 19 , $\sim 12.5 \text{ } 2\theta$).

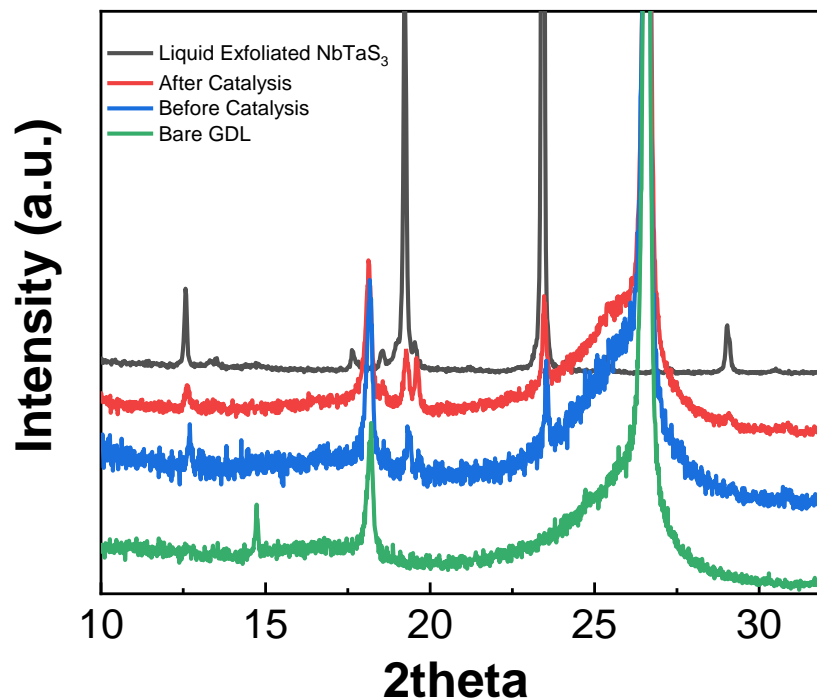


Figure S18. XRD pattern of the liquid exfoliated, exfoliated sample deposited on GDL before and after catalysis NbTaS₃ and bare GDL.

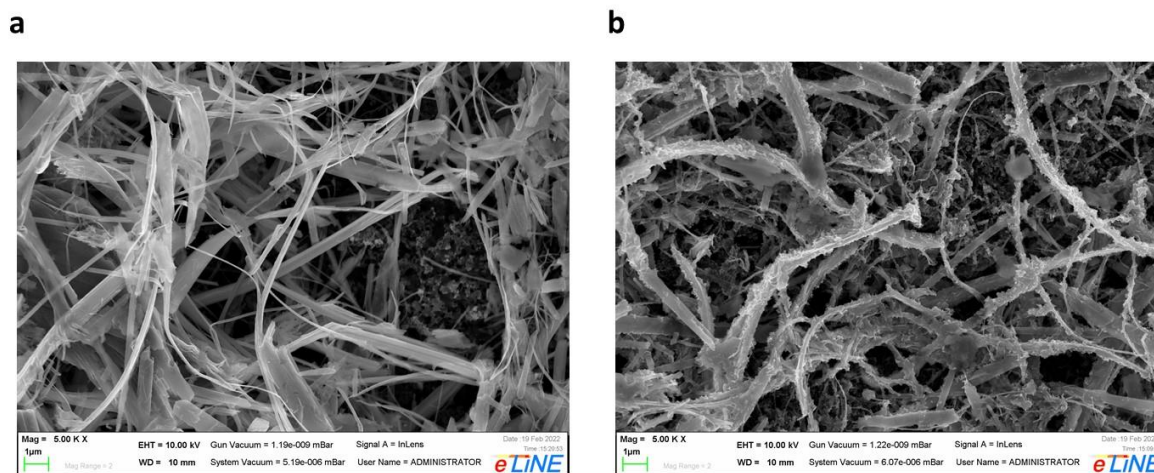


Figure S19. SEM images of electrode coated with Nb_{0.5}Ta_{0.5}S₃ fibers (a) pristine and, (b) after electrochemical CO₂RR experiments.

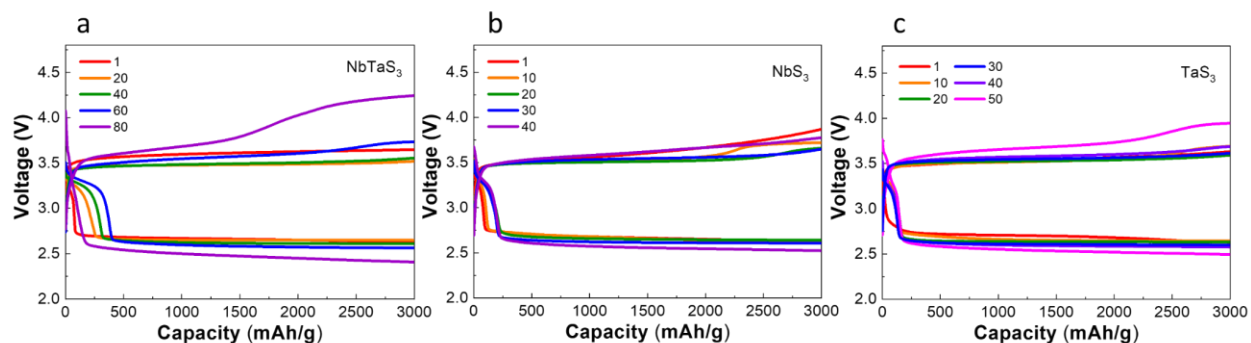


Figure S20. Battery cycling results with the cathodes of (a) $\text{Nb}_{0.5}\text{Ta}_{0.5}\text{S}_3$, (b) NbS_3 , and (c) TaS_3 nanofibers. The batteries were operated with a current density of 0.3 mA cm^{-2} and at cut-off voltage of 2.5 V.

S11. DFT calculations

DFT calculations were performed to further understand the reason for the enhanced electrochemical CO_2 reduction reaction. The bulk structure of $\text{Nb}_{0.5}\text{Ta}_{0.5}\text{S}_3$ was created from the structure has the unit cell of C-TaS3 (C2/m) published elsewhere^[5]. In order to determine lowest energy surface, 6 different facets terminated at either Nb or Ta or S were generated from the created bulk $\text{Nb}_{0.5}\text{Ta}_{0.5}\text{S}_3$ structure using the methods implemented in VirtualNanoLab (VNL) builder in QuantumATK - Atomistic Simulation Software^[6].

To determine the adsorption sites of CO_2 on $\text{Nb}_{0.5}\text{Ta}_{0.5}\text{S}_3$, first principles calculations were performed using Vienna Ab-initio Simulation Package (VASP)^[7-9] with plane wave basis sets and projector-augmented wave (PAW) pseudopotentials^[9]. The exchange-correlation functional were treated within the generalized gradient approximation (GGA) of Perdew-Burke-Ernzerhof (PBE)^[10]. The cutoff energy for the plane-wave basis was 600 eV, which was tested and applied for all supercells. The convergence criterion of the total energy was set to be within 1×10^{-6} eV within the K-point integration. The Brillouin zone was sampled at Γ -point only and all the geometries were optimized until the residual forces became less than 1×10^{-2} ($\text{eV}/\text{\AA}^2$).

We considered using Nb and Ta terminated (011) surfaces of $\text{Nb}_{0.5}\text{Ta}_{0.5}\text{S}_3$ as they were found to be comparably more stable surface among others, as shown in Table S2 and Figure S21. Furthermore, we performed DFT calculations on several possibilities of CO_2 adsorption on Nb terminated (011) surface. The initial and final structures, before and after relaxations showing adsorption of CO_2 at different sites, both oriented parallelly and perpendicularly on the surface, were studied and their configurations were shown in the Table S3. We did not observe any coordination between CO_2 and the sulfur surface. However, strong interactions were observed when OCOH^* or CO^* are placed on the Nb/Ta surface. More specifically, there was bond formation between Nb or Ta metal site of the surface to OCOH and CO , as shown in Table S4.

We then carried out the reaction energy profile for the reduction of CO_2 to CO on Nb/Ta terminated (011) surfaces. We computed reaction free energies of the reduction of CO_2 to CO , using computational hydrogen electrode based on Norskov electrochemical reaction theory approximations^[11]. As shown in Figure S22, calculated reaction free energies suggest that OCOH^* and CO^* formations are exergonic, both on Nb and Ta. Overall, our results suggest that formation of CO^* from CO_2 is more kinetically favorable on the Nb or Ta of the (011) surface.

Table S2. Surface energies (in $\text{eV}/\text{\AA}^2$) of different crystalline facets of $\text{Nb}_{0.5}\text{Ta}_{0.5}\text{S}_3$ calculated using DFT under different termination conditions. From the calculations, it was observed that crystal facet (011) with Nb termination is the most stable compared to other facets.

Termination \ Facets	Facets					
	001	010	011	100	110	111
Nb	0.036	0.020	0.018	0.049	0.020	0.019
Ta	0.036	0.020	0.019	0.049	0.019	0.021
S	0.036	0.019	0.020	0.037	0.020	0.020

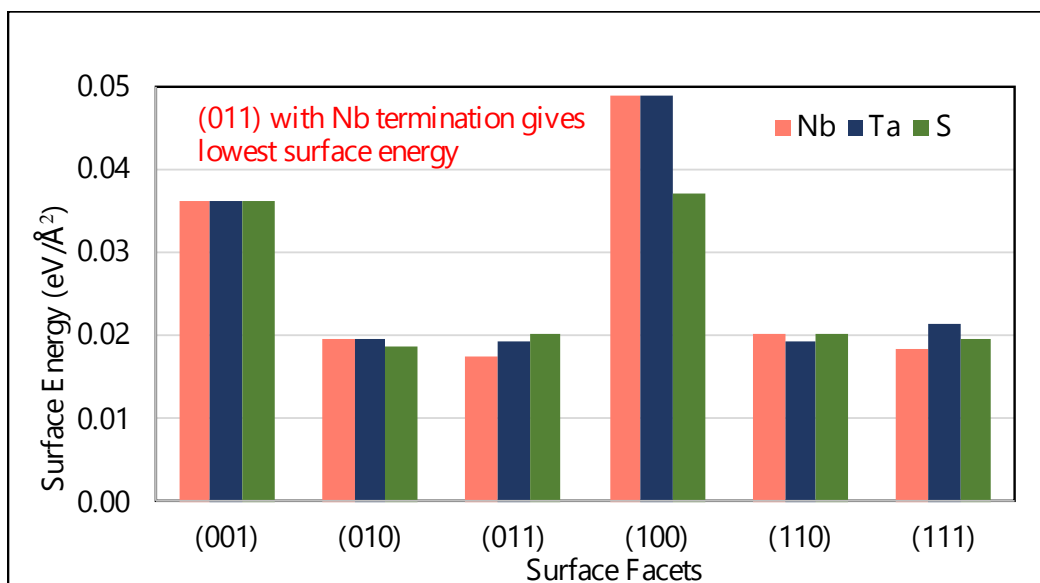
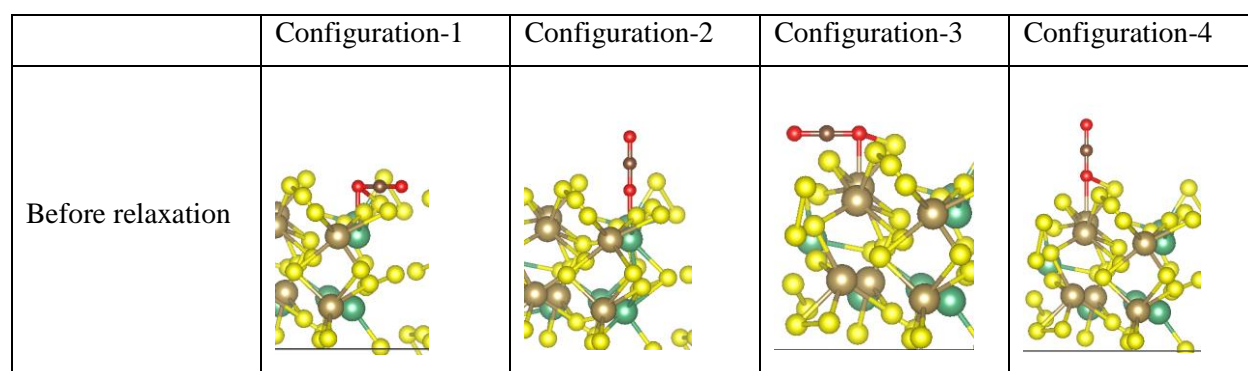


Figure S21. Surface energies (in $\text{eV}/\text{\AA}^2$) of different crystalline facets of $\text{Nb}_{0.5}\text{Ta}_{0.5}\text{S}_3$ calculated using DFT under different termination conditions. From the calculations, it was observed that crystal facet (011) with Nb termination is the most stable compared to other facets.

Table S3. Interaction between CO_2 and the (011) surface of $\text{Nb}_3\text{Ta}_3\text{S}_6$ were studied. Configurations 1 and 2 correspond to the orientation of CO_2 closer to the ‘Nb’ atom, in parallel and perpendicular to the surface, respectively. Configurations 3 and 4 correspond to the orientation of CO_2 closer to the ‘Ta’ atom, in parallel and perpendicular to the surface, respectively.



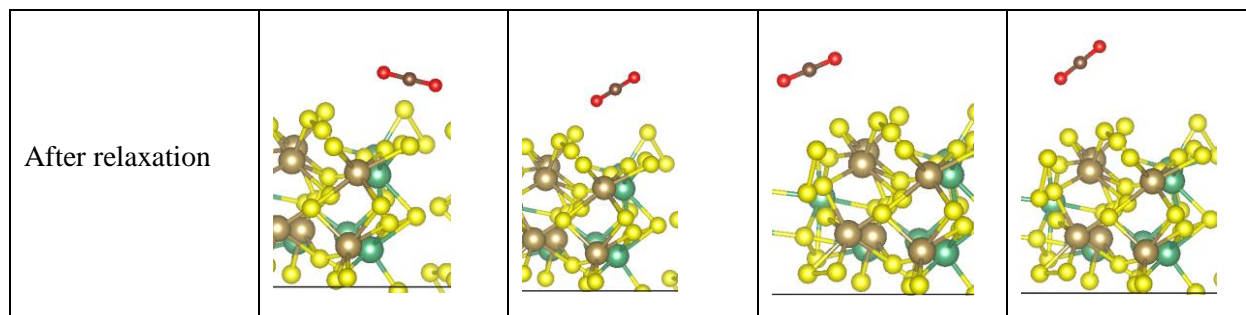
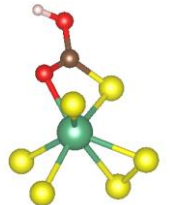
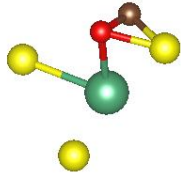
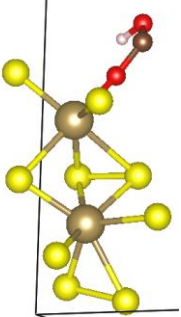
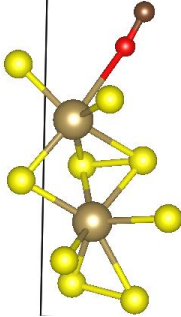


Table S4. Interaction between OCOH and CO on the (011) surface of $\text{Nb}_{0.5}\text{Ta}_{0.5}\text{S}_3$ were separately studied. OCOH or CO were initially placed closer to the ‘Nb’, or ‘Ta’ atoms of the surface, we observed that after relaxation, OCOH and CO formed bond with Nb or Ta, as shown below. Only the metal site of the surface that showed interactions with CO and OCOH are shown below for visualization purpose.

Adsorbed on	*OCOH	*CO
Nb		
Ta		

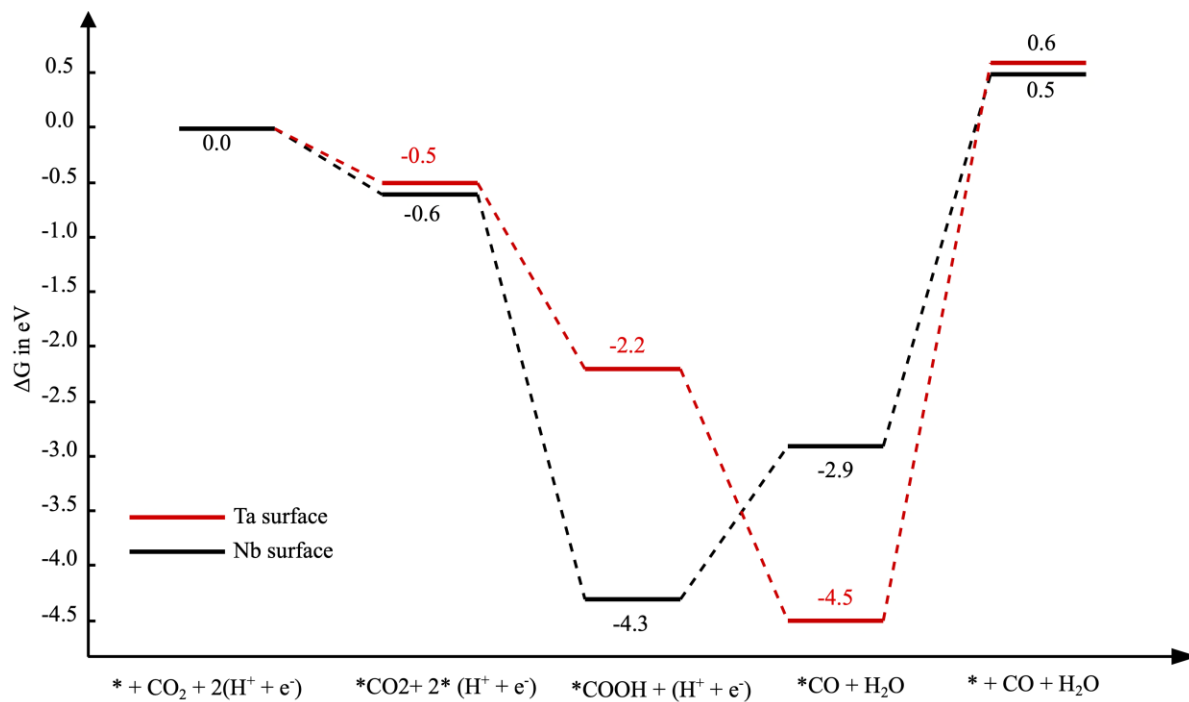


Figure S22. Reaction free energy profiles were studied on the reduction of CO₂ to CO on the (011) surface. Our results suggest that the adsorption is possible both on the Nb and Ta, and that they are exothermic.

Table S5. Comparison of state-of-the-art catalysts in electrochemical reduction of CO₂ towards CO

Catalyst	Potential (vs RHE)	Current density (mA/cm ²)	CO Faradaic efficiency (%)	Ref.
This work	-0.8	350	79	
WSe ₂	-0.76	330	86	[12]
MoS ₂	-0.76	65	98	[13]
Tri-Ag-NPs	-0.78	1.5	82	[14]
Ag NPs	-0.76	6.5	77	[15]
Ag bulk	-0.8	1.3	40	[16]
Au NPs	-0.8	4	63	[17]
Cu NPs	-0.75	1	3.5	[18]

Table S6. Comparison of state-of-the-art catalysts and electrolytes in Li-O₂ battery system.

Catalyst	Electrolyte	Current density (mA/cm ²)	Capacity (mAh/g)	Cycle life	Ref.
This work	InI ₃ /DMSO/IL	0.3	3000	80	
MoS ₂	LiTFSI/DMSO/IL	0.05	500	700	[19]
MoS ₂	InI ₃ /DMSO/IL	0.1	1000	200	[20]
Super P	DBDMB/LiCF ₃ SO ₃ /TEGDME	0.1	1000	100	[21]
CNT	TEMPO/IL/DEGDME	0.1	0.25 mAh cm ⁻²	20	[22]
Dye sensitized TiO ₂	Li/LiClO ₄ /DMSO	0.16	0.6 mAh	25	[23]
Carbon Fibers	FePc/LiTFSI/TEGDME	0.1	1000	130	[24]
Monolithic aerogel carbon paper	LiTFSI/LiBr/DEGDME	0.052	0.052 mAh cm ⁻²	30	[25]
Nano-Porous Gold	TTF/LiClO ₄ /DMSO	0.078	300	100	[26]
GO	LiTFSI/TTF/LiCl/DEGDME	0.1	1 mAh cm ⁻²	100	[27]
Ketjen Black	TEMPO/LiTFSI/Diglyme	0.1	500	50	[28]
XC-72R NORI	Li/LiTFSI/TEGDME	500 mA g ⁻¹	1000	100	[29]

Table S7. Comparison of breakdown current density, weight loss, and air stability of synthesized material with the state-of-the-art counterparts reported in literature

Breakdown current density	Weight loss at 800K in inert gas	Air stability sheet resistance at 40th day	Ref.
30 MA cm ⁻² (This work)	2% (This work)	40% increase (This work)	
1.7 MA cm ⁻² (TiS ₃)			[30]
0.4 MA cm ⁻² (Si NWs)			[30]
4.65 MA cm ⁻² (GaN NWs)			[31]
	20% (TiS ₃)		[30]
	8% (CNT)		[32]
	50% (TiO ₂)		[33]
		2100% (Ti ₃ C ₂ T _z)	[34]

References:

- [1] A. Meerschaut, L. Guemas, J. Rouxel, *J. Solid State Chem.* **1981**, 36, 118.
- [2] R. A. Gardner, M. Vlasse, A. Wold, *Inorg. Chem.* **1969**, 8, 2784.
- [3] S. A. Sunshine, J. A. Ibers, *Acta Crystallogr. Sect. C Cryst. Struct. Commun.* **1987**, 43, 1019.
- [4] L. Majidi, A. Ahmadiparidari, N. Shan, S. N. Misal, K. Kumar, Z. Huang, S. Rastegar, Z. Hemmat, X. Zou, P. Zapol, J. Cabana, L. A. Curtiss, A. Salehi-Khojin, *Adv. Mater.* **2021**, 33, 2004393.
- [5] C. C. Mayorga-Martinez, Z. Sofer, J. Luxa, Š. Huber, D. Sedmidubský, P. Brázda, L. Palatinus, M. Mikulics, P. Lazar, R. Medlín, M. Pumera, *ACS Nano* **2018**, 12, 464.
- [6] S. Smidstrup, T. Markussen, P. Vancraeyveld, J. Wellendorff, J. Schneider, T. Gunst, B. Verstichel, D. Stradi, P. A. Khomyakov, U. G. Vej-Hansen, M.-E. Lee, S. T. Chill, F. Rasmussen, G. Penazzi, F. Corsetti, A. Ojanperä, K. Jensen, M. L. N. Palsgaard, U. Martinez, A. Blom, M. Brandbyge, K. Stokbro, *J. Phys. Condens. Matter* **2020**, 32, 015901.
- [7] G. Kresse, J. Furthmüller, *Comput. Mater. Sci.* **1996**, 6, 15.
- [8] G. Kresse, J. Furthmüller, *Phys. Rev. B* **1996**, 54, 11169.
- [9] D. Joubert, *Phys. Rev. B - Condens. Matter Mater. Phys.* **1999**, 59, 1758.
- [10] J. P. Perdew, K. Burke, M. Ernzerhof, *Phys. Rev. Lett.* **1996**, 77, 3865.
- [11] A. A. Peterson, F. Abild-Pedersen, F. Studt, J. Rossmeisl, J. K. Nørskov, *Energy Environ. Sci.* **2010**, 3, 1311.
- [12] M. Asadi, K. Kim, C. Liu, A. V. Addepalli, P. Abbasi, P. Yasaei, P. Phillips, A. Behranginia, J. M. Cerrato, R. Haasch, P. Zapol, B. Kumar, R. F. Klie, J. Abiade, L. A. Curtiss, A. Salehi-Khojin, *Science* **2016**, 353, 467.
- [13] M. Asadi, B. Kumar, A. Behranginia, B. A. Rosen, A. Baskin, N. Reppin, D. Pisasale, P. Phillips, W. Zhu, R. Haasch, R. F. Klie, P. Král, J. Abiade, A. Salehi-Khojin, *Nat. Commun.* **2014**, 5, 1.
- [14] S. Liu, H. Tao, L. Zeng, Q. Liu, Z. Xu, Q. Liu, J.-L. Luo, *J. Am. Chem. Soc.* **2017**, 139, 2160.
- [15] C. Kim, H. S. Jeon, T. Eom, M. S. Jee, H. Kim, C. M. Friend, B. K. Min, Y. J. Hwang, *J. Am. Chem. Soc.* **2015**, 137, 13844.
- [16] L. Zeng, J. Shi, H. Chen, C. Lin, *Energies* **2021**, 14, 2840.
- [17] D. Kim, J. Resasco, Y. Yu, A. M. Asiri, P. Yang, *Nat. Commun.* **2014**, 5, 4948.
- [18] D. Kim, J. Resasco, Y. Yu, A. M. Asiri, P. Yang, *Nat. Commun.* **2014**, 5, 4948.

- [19] M. Asadi, B. Sayahpour, P. Abbasi, A. T. Ngo, K. Karis, J. R. Jokisaari, C. Liu, B. Narayanan, M. Gerard, P. Yasaei, X. Hu, A. Mukherjee, K. C. Lau, R. S. Assary, F. Khalili-Araghi, R. F. Klie, L. A. Curtiss, A. Salehi-Khojin, *Nature* **2018**, 555, 502.
- [20] S. Rastegar, Z. Hemmat, C. Zhang, S. Plunkett, J. Wen, N. Dandu, T. Rojas, L. Majidi, S. N. Misal, A. T. Ngo, L. A. Curtiss, A. Salehi-Khojin, *ACS Appl. Mater. Interfaces* **2021**, DOI 10.1021/acsami.0c15200.
- [21] Q. Xiong, G. Huang, X. B. Zhang, *Angew. Chemie - Int. Ed.* **2020**, DOI 10.1002/anie.202009064.
- [22] J. Zhang, B. Sun, Y. Zhao, A. Tkacheva, Z. Liu, K. Yan, X. Guo, A. M. McDonagh, D. Shanmukaraj, C. Wang, T. Rojo, M. Armand, Z. Peng, G. Wang, *Nat. Commun.* **2019**, 10, 1.
- [23] M. Yu, X. Ren, L. Ma, Y. Wu, *Nat. Commun.* **2014**, 5, 1.
- [24] D. Sun, Y. Shen, W. Zhang, L. Yu, Z. Yi, W. Yin, D. Wang, Y. Huang, J. Wang, D. Wang, J. B. Goodenough, *J. Am. Chem. Soc.* **2014**, 136, 8941.
- [25] W. J. Kwak, D. Hirshberg, D. Sharon, M. Afri, A. A. Frimer, H. G. Jung, D. Aurbach, Y. K. Sun, *Energy Environ. Sci.* **2016**, 9, 2334.
- [26] Y. Chen, S. A. Freunberger, Z. Peng, O. Fontaine, P. G. Bruce, *Nat. Chem.* **2013**, 5, 489.
- [27] J. Zhang, B. Sun, Y. Zhao, K. Kretschmer, G. Wang, *Angew. Chemie Int. Ed.* **2017**, 56, 8505.
- [28] B. J. Bergner, A. Schürmann, K. Pepler, A. Garsuch, J. Janek, *J. Am. Chem. Soc.* **2014**, 136, 15054.
- [29] S. Liao, Y. Dong, L. Leng, X. Zeng, F. Liu, L. Liu, G. Wang, L. Du, *Electrochim. Acta* **2016**, 200, 231.
- [30] A. J. Molina-Mendoza, J. O. Island, W. S. Paz, J. M. Clamagirand, J. R. Ares, E. Flores, F. Leardini, C. Sánchez, N. Agrait, G. Rubio-Bollinger, H. S. J. van der Zant, I. J. Ferrer, J. J. Palacios, A. Castellanos-Gomez, *Adv. Funct. Mater.* **2017**, 27, 1.
- [31] J. Qu, R. Wang, Y. Sun, I. Shih, Z. Mi, X. Liu, *Appl. Phys. Lett.* **2018**, 113, 193103.
- [32] M. S. Polyakova, T. V. Basova, *Macromolecules* **2017**, 50, 31.
- [33] A. Amarjargal, L. D. Tijing, C. S. Kim, *Ceram. Int.* **2012**, 38, 6365.
- [34] T. Habib, X. Zhao, S. A. Shah, Y. Chen, W. Sun, H. An, J. L. Lutkenhaus, M. Radovic, M. J. Green, *npj 2D Mater. Appl.* **2019**, 3, 8.